Radiometric Cross-Calibration of an Aerial Sensor with Satellite Top-of-Atmosphere Reflectance

Alexane Nghien[1], Manchun Lei[1], Mathieu Brédif[1], Olivier Hagolle[2]

[1] Univ Gustave Eiffel, ENSG, IGN, LASTIG, F-94160 Saint-Mandé, France – firstname.lastname@ign.fr
[2] CESBIO, Unité mixte CNES-CNRS-IRD-UPS, 31401 Toulouse Cedex 4, France - olivier.hagolle@cnes.fr

Keywords: Aerial sensor, Sentinel-2, cross-calibration, reflectance, Top-of-Atmosphere, atmospheric radiative transfer simulation

Abstract

Surface reflectance (SR) is essential for many remote sensing applications, but retrieving it from aerial images is challenging due to the lack of in-flight radiometric calibration and varying acquisition conditions. We propose a novel method for radiometric cross-calibration of aerial imagery using satellite Top-of-Atmosphere (TOA) reflectance. The method involves estimating at-sensor reflectance at the airborne altitude from satellite TOA reflectance, followed by spectral band adjustment and spatial alignment between satellite and airborne imagery. A linear radiometric model is derived to relate the Digital Number (DN) to the at-sensor reflectance from a selected subset of robust aerial-satellite pixel correspondences. The radiometric calibration parameter was retrieved using linear regression. The method is particularly suitable for airborne campaigns that lack onboard or in-situ radiometric calibration equipment. An ablation study is presented to analyze the selection of reliable reference pixels.

1. Introduction

Atmospheric correction aims to retrieve the Surface reflectance (SR) at the Bottom-of-Atmosphere (BOA) from remote sensing data by estimating and correcting atmospheric effects. Most biophysical/biochemical variable inversion algorithms are based on SR. It is also essential for change detection and land cover mapping. However, applying these atmospheric corrections on Top-of-Atmosphere (TOA) reflectance images relies on models that require calibrated sensors (with a temporally invariant response) and knowledge of acquisition conditions such as solar angles and atmospheric conditions (such as aerosol optical thickness) (Hagolle et al., 2017). The National Mapping Agencies produce nation-wide orthophotographs (images geometrically corrected with a uniform scale). However, the sun angle, atmospheric conditions, and sensor acquisition parameters change between images, causing color inconsistencies between images from a single acquisition mission and even larger inconsistencies between images from different acquisition missions, e.g. at the province boundaries.

In this article, we propose a novel method for radiometric cross-calibration of an airborne sensor using satellite TOA reflectance (here Copernicus Sentinel-2B (S2 Mission, 2017)). The first step of this work consisted of retrieving the reflectance at the airborne sensor altitude from the TOA reflectance given by the satellite data. The atmospheric radiative transfer equation (Vermote et al., 1997a) is expressed at the plane altitude to link the TOA reflectance to the reflectance at the airplane altitude. To apply the defined model, we simulated the atmospheric parameters in aerial conditions with the atmospheric radiative transfer model 6S (Vermote et al., 1997b) and the Py6S tool (Wilson, 2013). We used a linear transformation matrix to convert the spectral response of the satellite bands to that of the airborne sensor bands.

Moreover, aerial and satellite images do not have the same spatial resolution. In order to simulate aerial images at the satellite spatial resolution (60 cm to 10 m or 20 m), we use the Point Spread Function (PSF) of the Sentinel-2 by estimating the Gaussian PSF from the discrete values and applying it to the aerial spectral resolution. Then, an ablation study was conducted to identify the most reliable reference pixels from both the satellite and airborne imagery. Finally, we proposed a modified radiometric model (Lei et al., 2022) that relates the DN acquired from the aerial acquisition to the airborne at-sensor reflectance, estimated from the Sentinel-2 TOA reflectance.

2. Related work

Accurate radiometric calibration is essential for quantitative remote sensing applications. For satellite optical sensors, absolute radiometric calibration is typically performed using prelaunch laboratory equipment (Barker et al., 1984) and in-flight devices (Xiong et al., 2003), ensuring consistency and traceability of radiometric measurements. In contrast, aerial sensors are often calibrated using vicarious calibration methods (Biggar et al., 2003), such as ground-based reflectance targets or calibrated panels deployed during image acquisition (Markelin et al., 2008). However, such calibration setups are not always feasible, especially when dealing with large image archives acquired at different times and covering wide areas, where in-situ measurements become difficult or even impossible.

Relative Radiometric Normalization (RRN), which aims to align the radiometry of multi-temporal images. Notably, when the reference image is atmospherically corrected to surface reflectance, RRN can effectively align the subject image close to surface reflectance (Chen et al., 2010).

RRN assumes that a subset of pixels, known as Pseudo-Invariant Features (PIFs), exhibit stable reflectance characteristics over time and under varying acquisition conditions. The concept of PIFs dates back to (Schott et al., 1988), who first proposed using radiometrically stable pixels as references for inter-image normalization. Early approaches relied on manually selected features such as urban surfaces or water, which are assumed to maintain constant reflectance over time (Yuan and Elvidge, 1996). To improve automation and robustness, a method introduced in (Du et al., 2002) based on Principal Component Analysis (PCA) extracted PIFs in an unsupervised manner, providing a more data-driven and scalable approach to PIF detection. Building on these foundations, many studies have proposed increasingly robust strategies for PIFs selection, incorporating statistical modeling, spectral similarity, temporal consistency, or spatial homogeneity (Canty et al., 2004, Moghimi et al., 2021, Xu et al., 2021).

Inspired by these findings, we propose to extend the use of PIFs by identifying a subset of pixels whose radiometric values can be reliably used as references for vicarious calibration. Unlike traditional approaches that require in-situ measurements, we obtain the reference radiometric values directly from well-calibrated satellite observations, enabling cross-calibration between satellite and airborne sensors without the need for ground-based data (Bruegge et al., 2021).

Cross-calibration is traditionally used to ensure radiometric consistency between different satellite sensors (Claverie et al., 2018). Our work extends this framework to address the specific challenges of cross-platform calibration between satellite and airborne sensors. We tackle several new issues, such as the more significant spectral band mismatch, spatial resolution mismatch, and robust selection of reference pixels, which are especially pronounced between satellite and airborne sensors compared to inter-satellite calibration, and propose specialized solutions for each.

3. Radiometric cross-calibration method

3.1 Aerial reflectance retrieval from TOA reflectance

TOA reflectance can be expressed using the following analytical formula (Vermote et al., 1997b) :

$$\rho_{TOA}(\theta_s,\theta_v,\phi_s-\phi_v) = T^{\uparrow}_{g,TOA}(\theta_v)T^{\downarrow}_{g,TOA}(\theta_s)\Bigg[\rho_{R+A,TOA} + T^{\uparrow}_{TOA}(\theta_v)T^{\downarrow}_{TOA}(\theta_s)\frac{\rho_s}{1-S\rho_{s,Near}}\Bigg] \tag{1}$$

where θ_v and θ_s are the viewing and solar zenith angles, and ϕ_s and ϕ_v are the corresponding azimuthal angles. $\rho_{R+A,TOA}$ denotes the intrinsic reflectance of the molecular and aerosol layer; $T^{\uparrow}_{g,TOA}$ and $T^{\downarrow}_{g,TOA}$ represent the upward and downward gaseous transmittance, respectively; $T^{\uparrow}_{TOA}$ and $T^{\downarrow}_{TOA}$ are the upward and downward atmospheric transmittance; S is the total spherical atmospheric albedo; and F_0 is the extraterrestrial solar irradiance.

At the airplane altitude z, the reflectance at the sensor level can be written :

$$\rho_z(\theta_s,\theta_v,\phi_s-\phi_v) = T^{\uparrow}_{g,z}(\theta_v)T^{\downarrow}_{g,z}(\theta_s)\Bigg[\rho_{R+A,z} + T^{\uparrow}_{z}(\theta_v)T^{\downarrow}_{z}(\theta_s)\frac{\rho_s}{1-S\rho_{s,Near}}\Bigg] \tag{2}$$

We can combine equations (1) and (2) into a single expression. For fixed viewing and solar zenith angles θ_v and θ_s, and for each wavelength λ, we have:

$$\rho_z(\lambda) = A(\lambda)\rho_{TOA}(\lambda) + B(\lambda) \tag{3}$$

where

$$\begin{aligned} A(\lambda) =& \frac{T^{\uparrow}_{g,z}(\lambda)T^{\downarrow}_{g,z}(\lambda)T^{\uparrow}_{z}(\lambda)T^{\downarrow}_{z}(\lambda)}{T^{\uparrow}_{g,TOA}(\lambda)T^{\downarrow}_{g,TOA}(\lambda)T^{\uparrow}_{TOA}(\lambda)T^{\downarrow}_{TOA}(\lambda)} \\ B(\lambda) =& T^{\uparrow}_{g,z}(\lambda)T^{\downarrow}_{g,z}(\lambda)\Bigg(\rho_{R+A,z}(\lambda) \\ & - \frac{T^{\uparrow}_{z}(\lambda)T^{\downarrow}_{z}(\lambda)}{T^{\uparrow}_{TOA}(\lambda)T^{\downarrow}_{TOA}(\lambda)}\rho_{R+A,TOA}(\lambda)\Bigg) \end{aligned} \tag{4}$$

The previous equation establishes a linear relationship between the reflectance at any given altitude and the TOA reflectance across a continuous spectrum. By calculating the two coefficients $A(\lambda)$, $B(\lambda)$, one can convert the TOA reflectance to the reflectance at any altitude. However, since multispectral satellite sensors measure the integral of TOA reflectance over several spectral bands, we cannot directly discretize the previous equation. Therefore, we assume that the spectral-dependent parameters in the previous equation vary smoothly within the spectral band range. Under this assumption, the coefficients $A(\lambda)$ and $B(\lambda)$ can be separately integrated over the spectral bands, yielding scalar values A_Λ and B_Λ, which can then be used to compute the band reflectance $\rho_{z,\Lambda}$ at airplane altitude :

$$\rho_{z,\Lambda} \simeq A_\Lambda\rho_{TOA,\Lambda} + B_\Lambda \tag{5}$$

$$A_\Lambda = \frac{\int A(\lambda)f_\Lambda(\lambda)d\lambda}{\int f_\Lambda(\lambda)d\lambda}$$

$$B_\Lambda = \frac{\int B(\lambda)f_\Lambda(\lambda)d\lambda}{\int f_\Lambda(\lambda)d\lambda}$$

where $f_\Lambda(\lambda)$ is the Spectral Response Function (SRF) of the satellite sensor, and $\rho_{TOA,\Lambda}$ its measure of the TOA reflectance in band Λ.

3.2 Data reshaping

3.2.1 Spectral band adjustment Due to differences in the spectral coverage of the SRFs among sensors, Spectral Band Adjustment (SBA) is required to eliminate systematic errors in cross-sensor radiometric calibration (Teillet et al., 2007). For spectrally similar sensors (e.g., Landsat-8 OLI and Sentinel-2 MSI), it is generally sufficient to calculate the Spectral Band Adjustment Factor (SBAF) (Chander et al., 2013) between their most spectrally matched bands (e.g., OLI B2 blue band and MSI B2 blue band) to achieve cross-sensor bandpass adjustment (Claverie et al., 2018). This approach has also been widely applied for SBA between heterogeneous sensors, including Landsat 7 ETM+ and Terra MODIS (Angal et al., 2013), GaoFen-6 WFV and Sentinel-2 MSI (Han et al., 2022), as well as between the aerial photogrammetric sensor DMC and the spaceborne multispectral sensor MODIS (Harris and Van Niekerk, 2019).

Figure 1 compares the SRFs of the UltraCam sensor and Sentinel-2 MSI sensor. The UltraCam exhibits significantly broader spectral coverage than the MSI, with its SRFs spanning more than two MSI bands. Consequently, a single MSI band cannot adequately compensate for the radiometric response differences between the two sensors. To address this, we first simulated the band response values for both UltraCam and MSI using ECOSTRESS hyperspectral reflectance data (Meerdink et al., 2019). We then derived a linear transformation matrix from MSI to UltraCam bands using the Non-Negative Least Squares

https://doi.org/10.5194/isprs-archives-XLVIII-M-7-2025-49-2025 | © Author(s) 2025. CC BY 4.0 License.

(NNLS) method (Bro and De Jong, 1997). Separate transformation matrices were estimated for the S2A and S2B sensors. Table 1 presents the transformation matrices from the four 10-meter bands of Sentinel-2 to the four bands of the UltraCam. Table 2 summarizes the band-specific Root Mean Square Error (RMSE) of the estimated transformation.

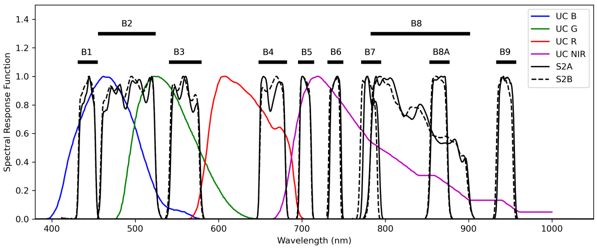

Figure 1. SRFs of UltraCam (UC) and Sentinel-2 A/B MSI bands. UC bands: Blue (B), Green (G), Red (R), and Near-Infrared (NIR) are represented by solid colored curves. Sentinel-2 bands: S2A (solid black) and S2B (dashed black) cover spectral ranges from 400–1000 nm (B1–B9). All SRFs are normalized to their peak response for comparison.

S2A to UltraCam Transfer Matrix

$$\begin{bmatrix} B \\ G \\ R \\ NIR \end{bmatrix} = \begin{bmatrix} 0.9712 & 0 & 0 & 0 \\ 0.3449 & 0.6581 & 0 & 0 \\ 0 & 0.2249 & 0.7749 & 0 \\ 0 & 0 & 0.2333 & 0.769 \end{bmatrix} \begin{bmatrix} B2 \\ B3 \\ B4 \\ B8 \end{bmatrix}$$

S2B to UltraCam Transfer Matrix

$$\begin{bmatrix} B \\ G \\ R \\ NIR \end{bmatrix} = \begin{bmatrix} 0.9716 & 0 & 0 & 0 \\ 0.3396 & 0.6635 & 0 & 0 \\ 0 & 0.2241 & 0.7757 & 0 \\ 0 & 0 & 0.2332 & 0.7691 \end{bmatrix} \begin{bmatrix} B2 \\ B3 \\ B4 \\ B8 \end{bmatrix}$$

Table 1. Spectral Transfer Matrices for S2A and S2B

	B	G	R	NIR
S2A	0.01749	0.00334	0.00671	0.01356
S2B	0.01724	0.00349	0.00686	0.01360

Table 2. Transformation RMSE from S2A/S2B to UltraCam bands

3.2.2 Spatial reshaping In order to create a corresponding dataset of DN from the aerial images and at-sensor reflectance estimated from the Sentinel-2 images, it was necessary to degrade the spatial resolution of the aerial images from 60 cm to 10 m, matching the spatial resolution of the satellite images. To achieve this, we used the PSF of Sentinel-2.

Each spectral band of the Sentinel-2 sensor has a corresponding PSF. As described in Section 3.2.1, the SBA from Sentinel-2 bands to UltraCam bands used a transformation matrix to linearly combine multiple Sentinel-2 bands. Accordingly, we also applied this transformation matrix to the PSFs of the Sentinel-2 bands in order to obtain a synthesized PSF corresponding to each UltraCam band.

For bands with a 10 m resolution, the PSF is provided by Sentinel-2 as a 33×33 grid at 2 m resolution, covering a spatial extent of 66 m × 66 m. The PSF follows a Gaussian shape. We estimated the parameters of the Gaussian function and resampled it to a PSF at 60 cm resolution, resulting in a 110×110 grid to be applied to the aerial images (Figure 2). Image borders are excluded, and only valid pixels are processed.

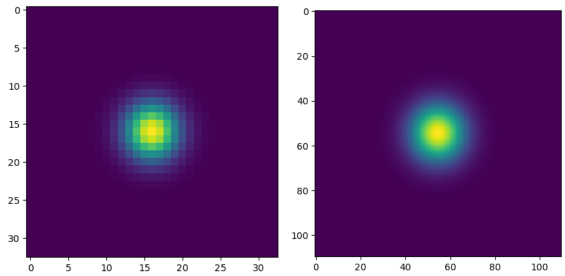

Figure 2. (Left) S2B B2 band PSF at 2 m resolution, (Right) Synthesized UltraCam blue band PSF at 60 cm resolution.

3.3 Calibration coefficient determination

The relationship between the DN acquired by the airborne imager and the incoming radiance can be expressed using the radiometric model proposed in (Lei et al., 2022) :

$$DN_\Lambda = \frac{\pi t}{4N^2} C_\Lambda S_\Lambda L_{z,\Lambda} + \varepsilon_\Lambda \tag{6}$$

where t is the exposure time (s), N is the f-number, L_z is the incoming radiance $(\mathrm{W} \cdot \mathrm{m}^{-2} \cdot \mu\mathrm{m}^{-1} \cdot \mathrm{sr}^{-1})$, C is the radiometric coefficient constant $(\mathrm{count} \cdot \mathrm{m}^2 \cdot \mu\mathrm{m}/\mathrm{J})$, S is the spatial variation factor and ε is the coefficient refers to dark current noise.

In the case of UltraCam sensor, we can assume :

- spatial variation within images is corrected by a vignetting calibration ($S_\Lambda = 1$)
- radiometric linearity is guaranteed
- dark current noise is corrected ($\varepsilon_\Lambda = 0$)

The relationship between the at-sensor reflectance and the incoming radiance is :

$$\rho_{z,\Lambda} = \frac{\pi L_{z,\Lambda}}{F_{0,\Lambda} cos(\theta_s)} \tag{7}$$

where F_0 the extraterrestrial solar irradiance.

The modified radiometric model for calibration is:

$$DN_\Lambda = \frac{t}{4N^2} C_\Lambda F_{0,\Lambda} \rho_{z,\Lambda} cos(\theta_s) \tag{8}$$

4. Experimentation

First, we applied the radiometric model to all aerial images acquired within 15 minutes before and after the satellite imaging to minimize differences in solar angles. Aerial images were downsampled to the spatial resolution of the satellite, while satellite images were transformed to the aerial at-sensor reflectance (section 3.1, 3.2).
Then we added some criteria to filter PIFs among all elements, to apply the radiometric model only on elements where the reflectance does not change between the aerial and satellite acquisition.

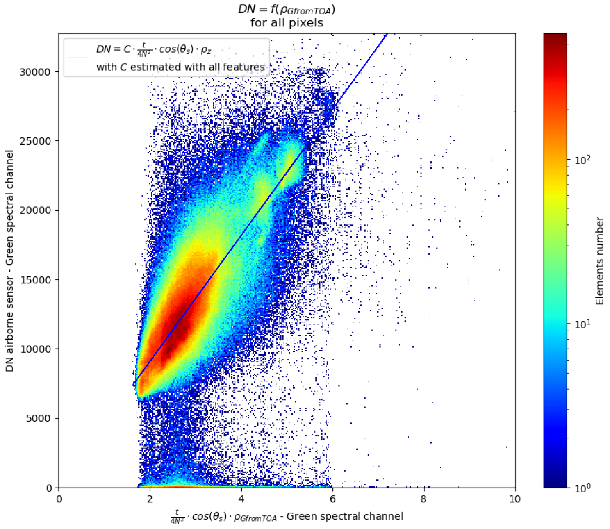

Figure 3. Radiometric coefficient retrieval using full pixels pairs for green channel

4.1 Cross-calibration using all pixels

For each spectral band, the radiometric coefficient C_Λ was estimated using the Random Sample Consensus (RANSAC) algorithm. To reduce the impact of the hot spot effect, an outlier filter was applied to remove extreme values. We fit the model on 80% of the dataset, and evaluate on 20%, randomly chosen. We computed the coefficient of determination R^2 and the Mean Absolute Percentage Error (MAPE) for each band. The results are presented in Figure 3 and Table 3. We remind that the coefficient of determination R^2 is defined as :

$$R^2 = 1 - \frac{SS_{residuals}}{SS_{total}} \tag{9}$$

Where $SS_{residuals}$ designates the sum of squares residuals and SS_{totals} the total sum of squares.

Band	**MAPE** in %	R^2	C_Λ
Blue	13358.53	0.0819	4704.4189
Green	7962.93	0.1349	4544.2405
Red	6874.08	0.3847	4780.4309
Near Infrared	5568.38	0.3774	6590.0969

Table 3. Cross-calibration results using full pixels pairs

4.2 Cross-calibration using PIFs

The results presented in Figure 3 and Table 3 indicate that using all pixels in the image pairs leads to a large number of outliers. These outliers are primarily caused by differences in the viewing geometry between aerial and satellite images. Aerial images typically have a wider field of view than satellite sensors. To mitigate the impact of these differences, we established a set of criteria for selecting PIFs, and evaluated their effectiveness through an ablation study and optimized their value by reducing the residuals in the calibration coefficient estimation.
Each criterion applied to the pixels reduces dratiscally the number of elements to apply the model to. Since we perform on aerial images of landscapes, it is not guaranted that for an optimized solution that we have enough elements to perform a robust calibration. In order to make sure we have enough PIFs to determine the calibration coefficient, we wanted to relax some criteria and only be restrictive on the most discriminant ones : we conducted an ablation study to chose which criteria to optimize the most.

4.2.1 Criteria to select PIFs

The criteria used to select PIFs are as follow :

Viewing direction difference. To remove directionnal effects, we only select pixels with the same viewing angles between aerial and satellite images. The viewing angle comparison is made using the angular distance between the corresponding viewing angles. The viewing angles of two images 1 and 2 are defined with (θ_1, ϕ_1) and (θ_2, ϕ_2). The angular distance between these viewing angles is calculated as follows :

$$\delta = cos^{-1}\Big(cos(\theta_1)cos(\theta_2) + sin(\theta_1)sin(\theta_2)cos(\Delta\phi)\Big) \tag{10}$$

Geometric difference (edge detection). Since the geometric registration of aerial and satellite images are not done at the same resolution and from the same DTM, misregistrations and misalignments may occur between the two images. To mitigate the impact of these misregistrations, we favor pixels in homogeneous areas by filtering out pixels with large gradient norm. Edge detection is performed using a simple Sobel filter on the two dimensional images. The edge strength values are normalized to the range [0, 1].

Change detection. We use the Multivariate Alteration Detection (MAD) (Nielsen et al., 1998) to detect spectral changes between two satellite images separated by large time intervals ($>$ 5 days). This algorithm relies on Canonical Correlation Analysis (CCA) to transform the multispectral image pair into a set of mutually uncorrelated difference components. Each component forms a change map. A threshold $|MAD|$ was applied to extract the no change area.

Removal of extreme values. To mitigate the hot spot effect, we removed extreme pixel values by discarding the top $k_{low}\%$ and bottom $k_{low}\%$ of the data distribution.

4.2.2 Ablation study

To better understand the contribution of each criterion and to find the most discriminant one to optimize it, we conducted an ablation study, where each parameter was removed individually, one at a time, based on proposed initial parameter values. As a measure, we calculate for each criterion the impact of this ablation in Table 4 as the difference of the R^2 scores between all criteria with the initialization values and without the studied criteria.

$$\begin{aligned} \text{Ablation Impact} = R^2_\Lambda \left(DN_{\Lambda,\text{full}}, \hat{DN}_{\Lambda,\text{full}}\right) - \\ R^2_\Lambda \left(DN_{\Lambda,\text{ablated}}, \hat{DN}_{\Lambda,\text{ablated}}\right) \end{aligned} \tag{11}$$

where the coefficient of determination R^2_Λ is a mean of each R^2 for the aerial spectral channels; `full` designates the PIFs filtered using all criteria; and `ablated` refers to the ones selected with one criterion omitted.

These results show that the solar angle and the filter of geometric differences have the most significant impact on the selection, whereas the change detection mask and the extreme values filter contribute less. Their ablation impact index is approximately ten times lower than that of the former two parameters.

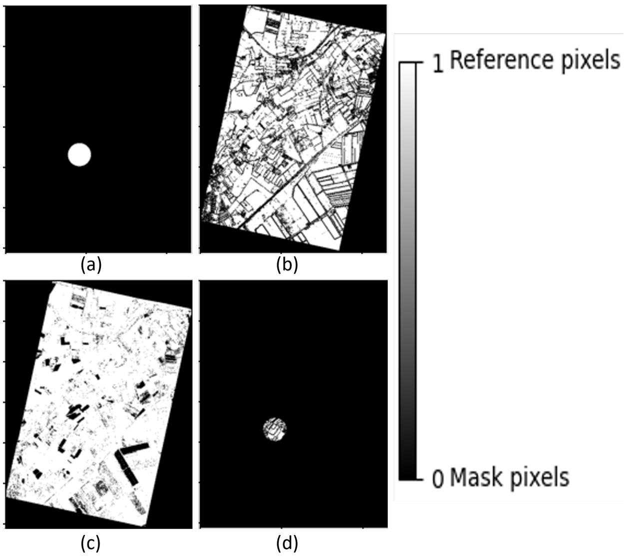

Figure 4. Binary masks for pixels of an aerial image (a) Angular condition; (b) Edges condition; (c) Change detection; (d) Reference features (intersection of all masks.

Parameter	Initial Value	Ablation Impact
δ Solar Angle	$2.5°$	0.261
$\|Grad\|$ Edges	0.5	0.141
$\|MAD\|$	0.5	0.011
k_{low} Extreme Low	2%	0.004
k_{high} Extreme High	98%	0.012

Table 4. Parameters initial value and ablation study impact

Each of the four previous filters used to select invariant features depends on a specific parameter. To optimize the choice of parameters, we started with empirical values (Table 4). Then, we optimized each parameter in turn, fixing the others.

4.2.3 Parameter optimization In order to find the optimal values for each parameter, we performed a semi-empirical optimization procedure. In this process, all parameters were fixed at their initial values except the one under optimization. We explored all possible values within a predefined interval, which is determined by the feasible range of the parameter, and calculated the evaluation criteria at each iteration.

$$1 - R^2_\Lambda \left(DN_{\Lambda,ref}, \hat{DN}_{\Lambda,ref} \right) \tag{12}$$

As for all pixels, the model is fitted on 80% of the PIFs dataset, and evaluated on 20% of it.

The optimal value for each parameter is defined as the one that minimizes the evaluation criterion. After optimizing all parameters, we reinitialize the system using the updated values. This process is repeated iteratively until the variation of parameters falls below 5%.

Figure 5 and 6 illustrate the variation of the R^2 score with respect to the difference of solar angle and edge detection. The results show that a smaller angular difference leads to a lower evaluation criterion, indicating improved performance. However, since multiple masks were overlaid to select PIFs, there were cases where no valid pixels could be detected in certain images. When the mask is too restrictive, the system becomes underconstrained. This is because the radiometric coefficient is estimated from a small subset of the reference data. It was therefore necessary to identify the limit where the system diverged.

The optimal semi-empirical parameter values used for extracting PIFs are presented in Table 5.

Parameter	Inital Value	Best Value	Max R^2
δ Solar Angle	$2.5°$	$1.43°$	0.9583
$\|Grad\|$ Edges	0.5	0.18	0.8809

Table 5. Summary of parameter study results

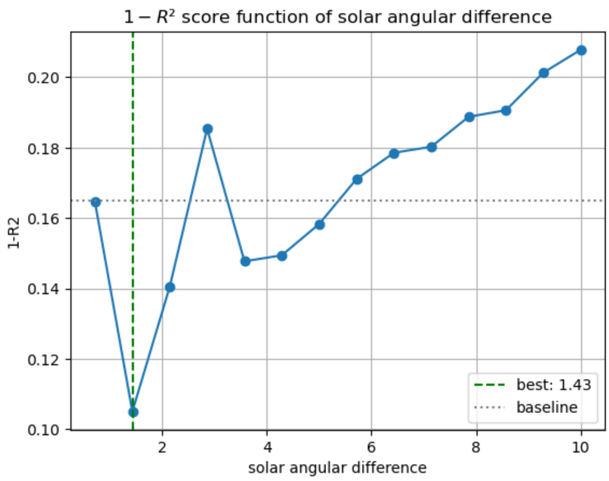

Figure 5. $1 - R^2$ error function of the angular acquisition difference between aerial and satellital image

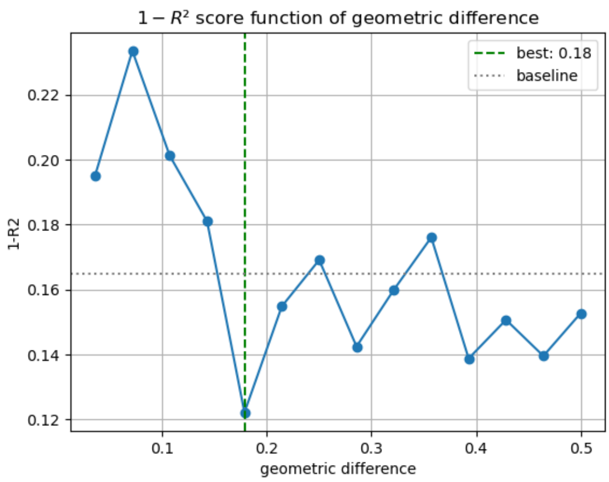

Figure 6. $1 - R^2$ error function of the geometric difference between aerial and satellital image

Finally we estimated the radiometric coefficient in Equation 8 with a RANSAC algorithm using only the PIFs (Figure 7), where the parameters t, N are provided by the aerial images metadata and the atmospheric parameter F_0 estimated through 6S (Wilson, 2013). The results show a significant improvement, as shown in Table 6 : the residuals error in percentage is much smaller when using the PIFs compared to using all pixels.

Band	MAPE in %	R^2	C
Blue	2.14	0.9263	4566.3554
Green	2.67	0.9082	4136.3551
Red	3.98	0.9539	4435.8575
Near Infrared	3.86	0.9516	6590.0969

Table 6. Comparison of calibrated sensors reflectance for PIFs

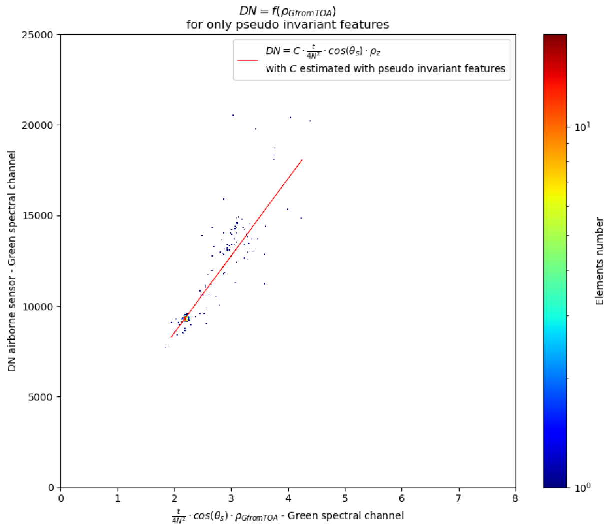

Figure 7. Radiometric coefficient retrieval using pseudo invariant pixels pairs for green channel

4.3 At-sensor reflectance retrieval

Then with these two coefficients estimated we can calibrate the sensor. with, for each aerial pixel i :

$$\rho_{\Lambda,i} = \frac{DN_{\Lambda,i}}{C_{\Lambda}.F_{0,\Lambda,i} \cdot \frac{t_i}{4N_i^2} \cdot cos(\theta_{s,i})} \tag{13}$$

where $F_{0,i}$ is estimated with the 6S code (Vermote et al., 1997b) and Py6S library (Wilson, 2013). We apply Equation 13 for the four aerial spectral bands for all aerial images with the same atmospheric conditions, to calibrate the sensor (Figure 8 as an example). This amounts to make a correspondence from digital numbers to reflectance.

5. Conclusion and perspectives

This study proposes an absolute radiometric cross-calibration method on airborne sensors, providing a reflectance value at the sensor-level in the viewing direction. Future work will consist in retrieving ground reflectance, removing the uniform atmospheric effect and the directional effect. Then we will be able to compute an absolute radiometric error evaluation.
The proposed calibration may be extended in several ways:

1. Improving what we qualify as a pseudo-Lambertian feature, the way we detect them (using bare ground detection), other algorithms than MAD.

2. This first calibration is made on a campaign where the aerial images acquired at the almost same time as the satellite acquisition. Further work will implement the same calibration on a larger dataset, not acquired at the same time and compare the quality of the coefficient determination and calibration.

3. Carrying out the calibration on images from overlapping aerial acquisitions. Actually, aerial images distant in time from the reference images used to calculate the coefficient can be a way to verify the impact of solar angle and other variations, such as the aerosol optical thickness variation, testing if it is still valid.

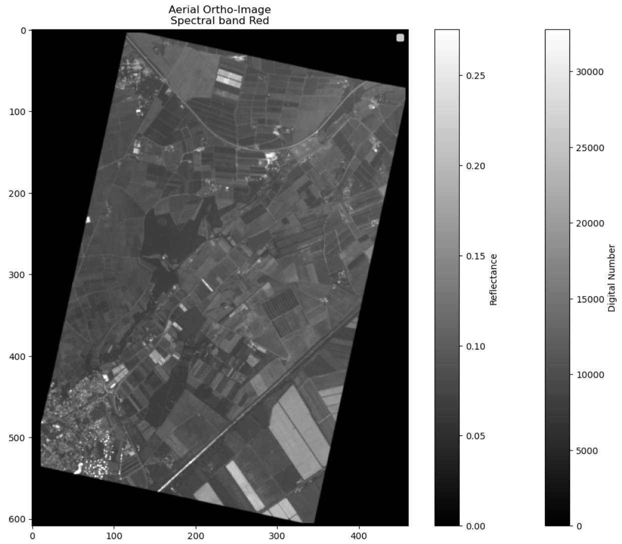

Figure 8. Aerial image before and after calibration for the red aerial spectral channel (input : digital numbers / output : reflectance)

References

Angal, A., Xiong, X., Wu, A., Chander, G., Choi, T., 2013. Multitemporal Cross-Calibration of the Terra MODIS and Landsat 7 ETM+ Reflective Solar Bands. *IEEE Transactions on Geoscience and Remote Sensing*, 51(4), 1870–1882.

Barker, J. L., Ball, D. L., Leung, K. C., Walker, J. A., 1984. Prelaunch absolute radiometric calibration of the reflective bands on the LANDSAT-4 protoflight Thematic Mapper. Technical Report NAS 1.15:85600.

Biggar, S., Thome, K., Wisniewski, W., 2003. Vicarious radiometric calibration of EO-1 sensors by reference to high-reflectance ground targets. *IEEE Transactions on Geoscience and Remote Sensing*, 41(6), 1174–1179.

Bro, R., De Jong, S., 1997. A fast non-negativity-constrained least squares algorithm. *Journal of Chemometrics*, 11(5), 393–401.

Bruegge, C. J., Arnold, G. T., Czapla-Myers, J., Dominguez, R., Helmlinger, M. C., Thompson, D. R., den Bosch, J. V., Wenny, B. N., 2021. Vicarious Calibration of eMAS, AirMSPI, and AVIRIS Sensors During FIREX-AQ. *IEEE Transactions on Geoscience and Remote Sensing*, 59(12), 10286–10297.

Canty, M. J., Nielsen, A. A., Schmidt, M., 2004. Automatic radiometric normalization of multitemporal satellite imagery. *Remote Sensing of Environment*, 91(3), 441–451.

Chander, G., Mishra, N., Helder, D. L., Aaron, D. B., Angal, A., Choi, T., Xiong, X., Doelling, D. R., 2013. Applications of Spectral Band Adjustment Factors (SBAF) for Cross-Calibration. *IEEE Transactions on Geoscience and Remote Sensing*, 51(3), 1267–1281.

Chen, W., Chen, W., Li, J., 2010. Comparison of surface reflectance derived by relative radiometric normalization versus atmospheric correction for generating large-scale Landsat mosaics. *Remote Sensing Letters*, 1(2), 103–109.

Claverie, M., Ju, J., Masek, J. G., Dungan, J. L., Vermote, E. F., Roger, J.-C., Skakun, S. V., Justice, C., 2018. The Harmonized Landsat and Sentinel-2 surface reflectance data set. *Remote Sensing of Environment*, 219, 145–161.

Du, Y., Teillet, P. M., Cihlar, J., 2002. Radiometric normalization of multitemporal high-resolution satellite images with quality control for land cover change detection. *Remote Sensing of Environment*, 82(1), 123–134.

Hagolle, O., Huc, M., Desjardins, C., Auer, S., Richter, R., 2017. MAJA Algorithm Theoretical Basis Document. Technical Report MAJA-TN-WP2-030 V1.0, Zenodo.

Han, J., Tao, Z., Xie, Y., Li, H., Guan, X., Yi, H., Shi, T., Wang, G., 2022. Radiometric Cross-Calibration of GF-6/WFV Sensor Using MODIS Images With Different BRDF Models. *IEEE Transactions on Geoscience and Remote Sensing*, 60, 1–11.

Harris, D., Van Niekerk, A., 2019. Radiometric homogenisation of aerial images by calibrating with satellite data. *International Journal of Remote Sensing*, 40(7), 2623–2647.

Lei, M., Thom, C., Meynard, C., Muller, J.-M., 2022. Calibration of a light hemispherical radiance field imaging system. *ISPRS Annals of the Photogrammetry, Remote Sensing and Spatial Information Sciences*, V-1-2022, 195–202.

Markelin, L., Honkavaara, E., Peltoniemi, J., Ahokas, E., Kuittinen, R., Hyyppä, J., Suomalainen, J., Kukko, A., 2008. Radiometric calibration and characterization of large-format digital photogrammetric sensors in a test field. *Photogrammetric Engineering & Remote Sensing*, 74(12), 1487–1500.

Meerdink, S. K., Hook, S. J., Roberts, D. A., Abbott, E. A., 2019. The ECOSTRESS spectral library version 1.0. *Remote Sensing of Environment*, 230, 111196.

Moghimi, A., Mohammadzadeh, A., Celik, T., Amani, M., 2021. A novel radiometric control set sample selection strategy for relative radiometric normalization of multitemporal satellite images. *IEEE Transactions on Geoscience and Remote Sensing*, 59(3), 2503–2519.

Nielsen, A. A., Conradsen, K., Simpson, J. J., 1998. Multivariate Alteration Detection (MAD) and MAF Postprocessing in Multispectral, Bitemporal Image Data: New Approaches to Change Detection Studies. *Remote Sensing of Environment*, 64(1), 1–19.

S2 Mission, 2017. https://sentiwiki.copernicus.eu/web/s2-mission.

Schott, J. R., Salvaggio, C., Volchok, W. J., 1988. Radiometric scene normalization using pseudo invariant features. *Remote Sensing of Environment*, 26(1), 1–16.

Teillet, P. M., Fedosejevs, G., Thome, K. J., Barker, J. L., 2007. Impacts of spectral band difference effects on radiometric cross-calibration between satellite sensors in the solar-reflective spectral domain. *Remote Sensing of Environment*, 110(3), 393–409.

Vermote, E. F., El Saleous, N., Justice, C. O., Kaufman, Y. J., Privette, J. L., Remer, L., Roger, J. C., Tanré, D., 1997a. Atmospheric correction of visible to middle-infrared EOS-MODIS data over land surfaces: Background, operational algorithm and validation. *Journal of Geophysical Research: Atmospheres*, 102(D14), 17131–17141.

Vermote, E. F., Tanre, D., Deuze, J. L., Herman, M., Morcrette, J. J., 1997b. Second simulation of the satellite signal in the solar spectrum, 6S: An overview. *IEEE Transactions on Geoscience and Remote Sensing*, 35, 675–686.

Wilson, R. T., 2013. Py6S: A Python interface to the 6S radiative transfer model. *Computers & Geosciences*, 51, 166–171.

Xiong, X., Chiang, K., Esposito, J., Guenther, B., Barnes, W., 2003. MODIS on-orbit calibration and characterization. *Metrologia*, 40(1), S89.

Xu, H., Wei, Y., Li, X., Zhao, Y., Cheng, Q., 2021. A novel automatic method on pseudo-invariant features extraction for enhancing the relative radiometric normalization of high-resolution images. *International Journal of Remote Sensing*, 42(16), 6153–6183.

Yuan, D., Elvidge, C. D., 1996. Comparison of relative radiometric normalization techniques. *ISPRS Journal of Photogrammetry and Remote Sensing*, 51(3), 117–126.